HHS Public Access

Author manuscript

J Biophotonics. Author manuscript; available in PMC 2019 April 01.

Published in final edited form as:

J Biophotonics. 2018 April ; 11(4): e201700268. doi:10.1002/jbio.201700268.

Spectrally Encoded Coherence Tomography and Reflectometry (SECTR): simultaneous *en face* and cross-sectional imaging at 2 gigapixels-per-second

Mohamed T. El-Haddad, **Ivan Bozic**, and **Yuankai K. Tao***

Department of Biomedical Engineering, Vanderbilt University, Nashville, TN 37235, USA

Abstract

Non-invasive biological imaging is crucial for understanding *in vivo* structure and function. Optical coherence tomography (OCT) and reflectance confocal microscopy are two of the most widely used optical modalities for exogenous contrast-free high-resolution three-dimensional imaging in non-fluorescent scattering tissues. However, sample motion remains a critical barrier to raster-scanned acquisition and reconstruction of wide-field anatomically accurate volumetric datasets. We introduce spectrally encoded coherence tomography and reflectometry (SECTR), a high-speed multimodality system for simultaneous OCT and spectrally-encoded reflectance (SER) imaging. SECTR utilizes a robust system design consisting of shared optical relays, scanning mirrors, swept-laser, and digitizer to achieve the fastest reported *in vivo* multimodal imaging rate of 2 gigapixels-per-second. Our optical design and acquisition scheme enable spatiotemporally co-registered acquisition of OCT cross-sections simultaneously with *en face* SER images for multi-volumetric mosaicking. Complementary axial and lateral translation and rotation are extracted from OCT and SER data, respectively, for full volumetric estimation of sample motion with micron spatial and millisecond temporal resolution.

Graphical abstract

A novel system design for a multimodal imaging system is presented. The system is designed for combined wide-field topographic and tomographic imaging at multi-gigapixel throughput, with potential applications in research and clinical settings. System performance is demonstrated through *in vivo* human imaging of the anterior chamber and the posterior retina. A preliminary algorithm is outlined that takes advantage of the three-dimensional motion information to perform multi-volumetric mosaicking of ultrawide-field retinal composites.

*Corresponding author: yuankai.tao@vanderbilt.edu.

Supporting Information: Additional supporting information may be found in the online version of this article at the publisher's website.

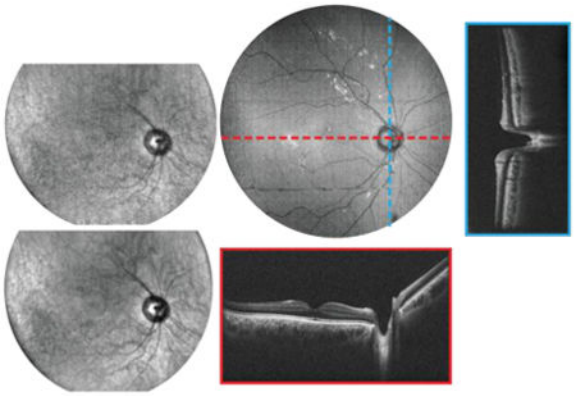

In vivo SECTR imaging of the human retina

Keywords

Imaging systems; Optical coherence tomography; Partial coherence in imaging; Three-dimensional image acquisition

1. Introduction

Non-invasive biological imaging is crucial for understanding *in vivo* structure and function. Optical coherence tomography (OCT) and reflectance confocal microscopy (RCM) are two of the most widely used optical modalities for exogenous contrast-free high-resolution three-dimensional imaging in non-fluorescent scattering tissues. OCT utilizes low-coherence interferometry to reject of out-of-focus light and measure depth-resolved backscattering profiles [1]. The high sensitivity and use of multiplexed detection in current-generation OCT [2–5] enable high-speed raster-scanned imaging with priority cross-sections acquired at several hundreds to thousands of frames-per-second (fps) and three-dimensional tomograms acquired at tens of volumes-per-second [6–9]. RCM provides high-contrast *en face* images of sample backscattering at up to 30 fps [10,11]. Whereas spectrally multiplexed detection in OCT allows simultaneous acquisition of all scatterer reflectivities in depth, tomographic imaging in RCM is achieved by serially stepping the focal plane with a minimum axial slice thickness determined by the confocal parameter [12]. Coherence-gated rejection of multiply scattered light and the high detection sensitivity of OCT also provide advantages for deep tissue imaging with up to 1-2 mm of penetration depth in densely scattering tissues [13] as compared to <300 μm in RCM [13–16]. However, despite the aforementioned advantages of OCT, RCM plays an important role in applications requiring high frame-rate *en face* imaging with minimal computational overhead, or in applications where subcellular imaging resolution is more favorable than penetration depth [13,17–19]. Additionally, while the superior contrast of fluorescence confocal microscopy has led to its broad adoption in basic sciences [20], the ability of RCM to resolve cellular and subcellular tissue structures without the need for exogenous contrast has made the modality uniquely suited for *in vivo* clinical diagnostic imaging [21,22].

Sample motion during *in vivo* imaging can significantly degrade image quality and fidelity. During volumetric acquisition, motion artifacts result in inaccurate three-dimensional reconstruction and limit the accuracy of quantitative data analysis. Higher imaging speeds reduce the effects of motion-induced artifacts, but suffer from inherent tradeoffs in signal-to-noise ratio (SNR), sampling density, and field-of-view (FOV). OCT systems with multi-MHz line-rates enable acquisition of densely sampled volumes over large FOVs [6,9,23]. However, at these line-rates, sufficiently high bandwidth spectral digitization is only achievable using broadband oscilloscopes, which precludes real-time image-processing and display.

Computational methods for volumetric motion correction that optimize a global error function over several serially acquired datasets have been previously published [24–27]. While this approach has been shown to remove motion artifacts in OCT volumes, it requires repeated volumetric sampling with orthogonal scan trajectories, the accuracy of the results depends on the number of repeated volumes, and use of overlapping mutual information results in a composite motion-corrected dataset that may not accurately represent the anatomic dimensions of the sample [24]. Thus, there remains a need for robust methods for post-acquisition sample motion correction. A recent approach demonstrated motion-corrected OCT using Lissajous scanning patterns that provided smooth, inherently overlapping trajectories [28]. While this eliminated the need for repeated orthogonal acquisitions, the requisite scanning protocol precluded real-time visualization of the acquired data and limited the utility for functional OCT extensions such as OCT angiography.

Other published approaches for motion-tracking and correction combine complementary spatial information from multiple imaging modalities for motion estimation and compensation. While combined OCT-RCM has been demonstrated for retinal imaging and motion-correction in post-processing [29], the video frame-rates of traditional RCM systems preclude imaging and tracking of high-speed sample motion and dynamics. Higher speed RCM can achieve several hundred frames-per-second imaging rates by using spinning disc or polygonal scanners [30–32]. However, these systems trade off FOV and sampling density and require bulky optics and complex scanning mechanisms, which are poorly suited for clinical translation.

Spectrally-encoded confocal microscopy (SECM) [33–35] addresses several key limitations of traditional RCM by parallel detection of sample backscattering using line-illumination. Wavelength-multiplexing lateral positions enables wide-field imaging at high frame-rates through simple fiber-optic based systems. Combined OCT-SECM has been demonstrated for volumetric co-registration using complementary *en face* and cross-sectional images for real-time *in vivo* aiming, and post-acquisition sample motion-tracking and compensation [36,37]. These previous-generation systems were limited by illumination and detection complexity, often requiring multiple light-sources and digitizers, each dedicated to one modality, or free-space bulk-optics spectrometers. Most importantly, SECM image quality was degraded by speckle noise as a result of interference effects from dense scatterers within each monochromatic spectrally-encoded focal volume.

We present spectrally-encoded coherence tomography and reflectometry (SECTR), a novel high-speed multimodal imaging system for simultaneous *en face* and cross-sectional imaging that overcomes limitations of traditional OCT-RCM. Spectrally-encoded reflectometry (SER) uses partially-coherent detection through a double-clad fiber (DCF) [38–40] to increase collection efficiency and reduce speckle-noise contrast at the expense of axial resolution as compared to conventional RCM. In addition, the DCF allows for single-mode illumination and multimode detection, which extends the confocal parameter without sacrificing lateral resolution [37]. Reflectance imaging using a large depth-of-focus is particularly advantageous for motion-tracking because it axially compounds different features from multiple depths into a single *en face* frame for image registration. However, while DCFs have been utilized in both fluorescence and reflectance imaging applications [39,41–44], the benefits of DCF in applications with strict low-incident-power limits, such as ophthalmic imaging, have been limited because inner-clad back-coupling of end-face reflections results in a large background signal, thereby reducing the available detection dynamic range and SNR [37,45,46]. In SECTR, we introduce a novel fiber termination scheme that mitigates end-face reflections by more than an order-of-magnitude, enabling direct-detection of *en face* sample scattering through a DCF.

We also reduce the system complexity of previously described multimodality imaging systems to benefit translation of our technology for research, commercial, and clinical applications. In SECTR, OCT and SER share a swept-laser source, a scan mirror, a digitizer, imaging optics, and triggering and clocking electronics. The resulting system allows for multimodality imaging of inherently spatiotemporally co-registered fields with a net throughput of 2 gigapixels-/4 gigabytes-per-second. High-speed volumetric OCT provides depth-resolved micron-resolution visualization of subsurface features-of-interest with high SNR, whereas complementary *en face* SER provides anatomical landmarks that enables aiming, sample positioning, motion-tracking, and multi-volumetric mosaicking of ultrawide-field datasets.

As a proof-of-concept, we combined SECTR with imaging optics optimized for wide-field imaging in the posterior retina and anterior chamber of the human eye. *In vivo* ophthalmic imaging allows for comprehensive assessment of imaging system performance and utility because 1) incident light levels are limited by established maximum permissible exposure (MPE) standards and, thus, requires high imaging dynamic range and SNR; 2) the fast dynamics of micro-saccadic eye movements, which are on the order of 100-200 Hz [47], may be used to evaluate the temporal resolution and spatial accuracy of SER motion-tracking; and 3) OCT is a well-established ophthalmic imaging technology with broad applications in diagnostics and therapeutic guidance. At the maximum sampling rate, 5 megapixel *in vivo* OCT and SER images were simultaneously and continuously acquired at 200 fps. Using complementary OCT and SER feature points, we also demonstrate multi-volumetric registration and widefield mosaicking. Our results show that SECTR addresses unmet needs in *in vivo* imaging and motion-tracking to provide anatomically accurate, densely-sampled volumetric datasets of sample scattering over large FOVs. We believe the utility of our imaging platform extends beyond ophthalmic imaging and is broadly applicable for wide-field optical imaging with high temporal resolution.

2. Methods

2.1 Engine

A 200 kHz, 63% duty cycle swept-laser source (SSOCT-1060, Axsun) was optically buffered through a 500 m fiber spool (HI1060, Corning) to achieve 100% duty cycle at 400 kHz sweep-rate (Fig. 1(a)). The laser output was split into two copies and one coupler output was relayed through the fiber spool, which corresponded to a half sweep period delay. Both the original and delayed copies of the sweep were then recombined using a 50:50 coupler, effectively doubling the sweep-rate. The buffering stage input was asymmetrically split by a 53:47 fiber coupler (AC Photonics), to compensate for losses in the fiber spool. Polarization controllers were used in both arms of the buffering stage to minimize polarization mode dispersion and achieve an optimal OCT point-spread function (PSF) [48]. The unbuffered laser had a 3-dB optical bandwidth of 105 nm centered at 1060 nm, which was reduced to approximately 83 nm useable bandwidth after buffering because of spectral overlap between original and buffered sweeps.

One output from the buffering stage was split between the OCT and a Mach-Zehnder interferometer (MZI) for k-clock generation using a 90:10 coupler, and the OCT output was split into reference and sample arms using a 70:30 coupler, respectively. The reflective reference arm included a broadband fiber circulator (AC Photonics), and polarization controllers used to match sample and reference polarization to maximize OCT SNR.

The second output from the buffering stage was split between the SER and a fiber Bragg grating (FBG) for optical triggering using a 95:5 coupler. SER illumination was coupled to a DCF by fusion-splicing the 95% coupler output to the single-mode input of a prototype DCF coupler (DC1060LEB, Castor Optics/Thorlabs). Here, the core of the DCF was used for single-mode SER illumination and the inner-cladding was used for multimode detection.

2.2 Optomechanical layout

SECTR reduces the size and complexity of traditional multimodal OCT and RCM systems and ensures spatiotemporal registration by using a shared galvanometer mirror (OCT fast-axis and SER scan-axis) and imaging relay (Fig. 1(b)). SER illumination from the single-mode core of the DCF was collimated to a 9.5 mm spot using two achromatic doublets with a combined focal length of 25.2 mm, and dispersed through a 1379 lines/mm polarization independent transmission grating (PING-Sample-420, Ibsen Photonics). The grating was imaged onto the face of the shared galvanometer scanner (G_x) through a 1.9x demagnifying 4-f relay (Fig. 1(b), f_{obj} and f_r), and then demagnified again by a shared 2.6x 4-f relay (Fig. 1(b), f_s and f_{oph}) to a 1.9 mm spot at the pupil plane. OCT illumination was collimated using an 18 mm focal length triplet collimator (TC18-1064, Thorlabs) to a 5.2 mm spot, scanned by the OCT slow-axis galvanometer (G_y), and demagnified across a 1.3x (Fig. 1(b), f_s and f_R) and the shared 2.6x (Fig. 1(b), f_s and f_{oph}) 4-f relay to a 1.6 mm spot at the pupil. OCT and SER beams were combined at the focal planes of their respective relay telescopes across two adjacent faces of a custom prism mirror (Fig. 1(b), PM). The mirror was designed with an apex angle of 157.5° to colinearly combine the reflected output of OCT and SER optical paths oriented at 45° angular separation. The prism mirror was used in place of a

beamsplitter to maximize optical throughput, and the OCT and SER paths were focused onto opposite sides of the apex to minimize spatial separation between their respective fields (340 μm at the image plane).

2.3 Suppression of DCF end-face reflection back-coupling

The major limitation of illumination and collection through the core and inner-cladding of DCFs, respectively, is the strong fiber end-face reflection that dominates sample backscattering in direct-detection modalities such as RCM and SER (Fig. 1(c)). Conventional fiber termination methods, such as angled physical contact, preferentially couple end-face reflections into the clad and result in higher background signals for DCFs as compared to flat-polished terminations. We mitigate end-face reflections by index-coupling a flat-polished DCF to the flat face of a wedge prism (Fig. 1(c), middle and right). By optimizing the wedge prism thickness and angle, we spatially offset the dominant glass-air interface reflection to minimize coupling into the DCF inner-clad (Fig. 1(c), right). ZEMAX simulations showed a minimum required wedge prism base thickness of 1 mm and angle of 10° for a DCF with 0.14 core numerical aperture and 105 μm inner-clad diameter. Using a wedge prism with 3 mm base thickness and 11.2° angle (PS812-B, Thorlabs), we measured a 12.5x reduction in back-coupled end-face reflections (Fig. S1).

2.4 Optical performance and sampling requirements

SECTR design was optimized and performance was simulated using ZEMAX, and the Pomerantzeff eye model was used to evaluate optical performance at the retina [49]. On-axis OCT and the central 23° SER field spot-sizes were diffraction-limited with an Airy radius of 13 and 10.5 μm, respectively (Fig. 2). In addition to spot-size, SER resolution along the spectrally-encoded dimension was also dependent on the number of resolvable spots (N_r) at the grating. For a 9.5 mm collimated spot, our grating resolved a maximum of 1831 spectral channels across the full 105 nm bandwidth of our unbuffered laser sweep. Spectral overlap after optical buffering reduced the useable bandwidth, and consequently reduced the number of resolvable spots to 1447. Thus, at 400 kHz buffered sweep-rate, a >1.16 GHz clock was required to critically sample the SER signal.

2.5 Triggering and clocking

SECTR imaging was synchronized to the laser sweep-rate using an optical trigger. Five percent of the SER arm from the buffering stage was coupled to a 1017.06±0.08 nm FBG (O-E Land) with 95% reflectivity. The reflection from the FBG was detected with a 250 MHz InGaAs PIN photodiode (FPD510-F, MenloSystems) and amplified with a 1.6 GHz 37 dB electronic amplifier (ACA-2, Becker & Hickl) to provide a wavelength-specific trigger for a shared high-speed digitizer. The auxiliary channel of the digitizer was configured to output an electronic TTL signal synchronized to the optical trigger and used to trigger galvanometer scan waveforms generated with a digital-to-analog converter (PCI-6221, National Instruments).

An external MZI was used to generate a second optical clock for linear-in-k sampling of each laser sweep. The MZI path-length mismatch was set to generate a 600 MHz fringe frequency that was detected on a 1.6 GHz balanced photodiode (APD481-AC, Thorlabs),

high-pass filtered (SHP-400+, Mini-Circuits), and conditioned using an analog comparator (ADCMP565, Analog Devices). The comparator output was then electronically doubled [50] and the output signal was amplified (ZKL-2+, Mini-Circuits), band-pass filtered between 395-700 MHz (SHP-400+ and SLP-750, Mini-Circuits), and frequency-doubled (FK-5-S, Mini-Circuits). Finally, the signal was band-pass filtered between 1000-1400 MHz (SHP-950+ and SLP-1650+, Mini-Circuits), resulting in a stable 1.2 GHz k-clock for linear-in-wavenumber and Nyquist sampling of OCT and SER signals. However, due to data-alignment and triggering constraints inherent to the digitizer used, each 400 kHz sweep was sampled with 2560 samples-per-sweep instead of the maximum 3000 samples-per-sweep, which resulted in a combined OCT and SER throughput of 2 gigapixels-per-second (Supplementary Note 5).

2.6 Detection, acquisition, and phase-alignment

SECTR signals were acquired using a 12-bit dual-channel 4 GS/s digitizer (AT-9373, AlazarTech). The OCT signal was detected using a 1.6 GHz balanced photodiode (APD481AC, Thorlabs). A 1083.08±0.123 nm FBG with 99.94% reflectivity (O-E Land) was coupled to one input of the balanced photodiode to generate a reference peak in the detected OCT interferogram [51]. In post-processing, this peak was used to spectrally align both OCT and SER samples to measure trigger fluctuation, compensate for inherent sweep-to-sweep jitter, and eliminate coherent noise artifacts from OCT data [50,52]. Coaxial cable lengths for the OCT and k-clock were matched to avoid depth-dependent degradation of the OCT axial PSF due to phase errors [50].

Backscattered SER light was collected through the inner cladding of the DCF and detected through the multimode arm of the DCF coupler using a 2.2 GHz amplified photodiode (RIP1-JJAF, Voxtel). The photodiode output signal was amplified with a 20 dB electronic amplifier (ZFL-500, Mini Circuits) and sampled using one channel of the high-speed digitizer. SER data was acquired simultaneously with OCT on the second channel of the shared digitizer. Multimode collection using the DCF increased optical throughput by >3.5x and reduced speckle contrast by >3.6x as compared to single-mode [37].

C++ software was developed for acquisition, processing, display, and data archival at a total data throughput rate of 4 GB/s. Data was streamed to a high-speed RAM disk (800 MHz DDR3), which allowed up to 10 seconds (40 GB) of continuous acquisition. Circular buffering was not performed to avoid data loss; acquisition time was limited by the available RAM disk space. The data was sub-sampled, processed, and displayed live at 17 fps for real-time aiming and alignment. A background frame was obtained with each acquisition to subtract the DC spectral shape of the source from the OCT and the SER frames. Numerical dispersion compensation was performed on each OCT frame [5].

2.7 Multi-volumetric mosaicking

A custom semi-automatic algorithm was developed for multi-volumetric registration of overlapping retinal datasets into an ultrawide-field mosaic. SECTR frames were pre-processed to correct for bulk-motion in the axial and lateral planes, using OCT and SER

data, respectively. OCT cross-sections were then flattened to eliminate tilt and curvature variations in retinal layers and enable volumetric mosaicking (Fig. S3).

Global non-rigid transformations between the SER frames, corresponding *en face* OCT projections, and overlapping volumetric datasets were automatically calculated using spline transformations based on automatically-extracted anatomical landmarks [53]. Vascular features were first enhanced using a Gabor kernel at various orientations. A skeletonized map of the vasculature was then generated and convolved with a dictionary of predefined 3x3 neighborhood kernels to automatically identify the branching points, which were used as landmarks for the non-rigid registration. The only manual step in our processing algorithm was the addition of choroidal vasculature branching points and intersections between retinal and choroidal vascular projections to improve the registration accuracy. All SECTR volumes were registered to one central volume.

Accuracy of the mosaicking output was quantified using cross-correlation of the overlapping regions of the adjacent volumetric datasets. In locations with more than two overlapping volumes, a global coefficient was calculated as the arithmetic mean of all the calculated coefficients.

3. Results

3.1 Optical performance

SECTR optical performance was evaluated by imaging a USAF-1951 resolution test chart at the intermediate image plane before the ophthalmic lens (Fig. 1(b), f_{oph}). ZEMAX simulated lateral resolution in this plane for OCT and SER were 37 and 30 μm, respectively. Imaging results showed that OCT could resolve 35 μm features and SER could resolve 39 μm and 28 μm features in its spectrally-encoded and scanned dimensions, respectively (Fig. 3).

3.2 OCT sensitivity and axial resolution

OCT had a measured SNR of 96 dB with 1.3 mW of incident power. The -6 dB fall-off depth was 7.5 mm and full imaging range was 9.56 mm when sampled using the 1.2 GHz k-clock (Fig. 4(a)). The axial resolution, measured using a calibrated reflector, was 11.2 μm full-width at half-maximum (FWHM) at 500 μm from the zero delay in air and did not degrade significantly over the full imaging range (Fig. 4 (b), (c)).

3.3 In vivo human ophthalmic imaging

In vivo SECTR imaging was demonstrated in a healthy volunteer under an IRB-approved protocol. The optical power incident at the pupil was 1.3 mW for OCT and 2.65 mW for SER, which was well below the American National Standards Institute (ANSI) MPE limits for combined point-scanning and extended source illumination at 1060 nm light [54] and less than that used in previously published systems [37,55].

A >45° (15 mm diameter) FOV on the posterior retina (Fig. 5) and anterior segment (Fig. S4) was imaged simultaneously with OCT and SER. OCT volumes were sampled with 2560 × 2000 × 1400 pix. (spectral × lateral × lateral) in 7 s, and corresponding SER images were sampled with 2560 × 2000 pix. (spectral × lateral) at 200 fps. High frame-rate SER images

provided *en face* views of anatomic structures for aiming and fixation and showed sample motion dynamics from saccades (retina) and pupil dilation (iris). Retinal OCT cross-sections clearly showed tissue layers, the fovea, and the optic nerve. The cornea, iris, and anterior lens capsule were also clearly resolved on anterior segment OCT. Comparison of respective anatomic landmarks between *en face* OCT volume projection and SER images showed spatiotemporal co-registration of overlapping FOVs (Visualizations 1 and S2).

3.4 Ultrawide-field volumetric mosaicking

Video-rate visualization of *en face* SER provided real-time feedback for multi-field aiming and acquisition, and allowed for accurate positioning of the sample to achieve desired overlap for mosaicking (Fig. 6(a)). Nine datasets were acquired at various retinal eccentricities with 50% overlap between the adjacent fields, and mosaicked in post-processing. Figure 6 shows sub-fields and multi-volumetric mosaics of corresponding SER and OCT data from overlapping SECTR volumetric datasets, respectively. *En face* sub-fields (Fig. 6 (a), (d)) are shown after registration and non-rigid transformation. Multi-volumetric mosaics (Fig. 6 (b), (e)) show artifact-free ultrawide-field images over a 90° FOV.

Cross-correlation coefficient maps were used to verify the mosaicking accuracy (Fig. 6 (c), (f)). In both cases, the cross-correlation value was between 0.94 and 0.97 over the entire FOV. Figure 7 shows an enlarged *en face* OCT projection, of the multi-volumetric mosaic, together with representative fast- and slow-axis cross-sections.

En face visualizations of the retinal pigment epithelium (RPE) and the choroid layers show shadowing from retinal (Fig. 8(a)), and choroidal (Fig. 8(b)) vasculature, respectively, and provide qualitative measures for mosaicking accuracy.

4. Discussion

4.1 SER optical performance

Optical performance characterization showed astigmatism in the SER focal plane (Fig. 3). To compare lateral resolution with ZEMAX simulations, the USAF-1951 resolution test chart was imaged at slightly offset image planes, each optimized for lateral resolution in either the spectrally-encoded or raster-scanned dimension. In *in vivo* imaging, the ophthalmic lens (Fig. 1(b), f_{oph}) was positioned to optimize overall image quality. The astigmatism was not inherent to the optical design but rather a result of bulk-optics alignment error between the two SER imaging relays (Fig. 1(b), f_c-f_{obj} and f_r-f_s).

In addition to astigmatism, our results also showed differences between SER lateral resolutions in the spectrally-encoded and raster-scanned dimensions. This was attributed to dominant chromatic aberration, which maps to spherical aberration in SER. This effect was magnified in the characterization plane because the system was designed for optimal performance in the eye. Characterization of imaging performance in an intermediate image plane without the ophthalmic lens (Fig. 1(b), f_{oph}) and eye removes significant longitudinal chromatic aberration that was not otherwise compensated. Thus, *in vivo* results have expectedly better resolution.

4.2 Data throughput considerations

At the optimal source duty cycle, the required sampling rate would increase to approximately 2 GHz, which approaches the speed limit of state-of-the-art digitizers. In addition, an 8-lane PCI-express 3 bus is limited to <7 GB/s of data throughput and fundamentally limits digitizer readout speeds at full bit-depth. However, data throughput limitations may be overcome by reducing imaging bit-depth, which has been previously shown to not significantly impact swept-source OCT SNR [56]. Another potential limitation to higher clock-rates is the capacity to store data. In this demonstration, SECTR data were streamed to computer memory that was benchmarked at >10 GB/s throughput. However, expanding memory to increase total acquisition duration becomes prohibitively expensive. RAID0 striping of high-speed solid-state drives (SSDs) or PCI-express SSDs, which are capable of sustained write-speeds of >4 GB/s, may be a cost-effective alternative fast storage solution.

4.3 Ultrawide-field volumetric mosaicking

Three-dimensional acquisition using SECTR enables aiming, motion-tracking (Fig. S2) and multi-volumetric registration and mosaicking, as demonstrated in our preliminary results. Partially-coherent SER detection provides more anatomical features and allows for more accurate and robust registration as compared to coherent detection.

The described algorithm for segmentation and flattening of the RPE (Fig. S3) was robust against variations in the retinal curvature and tilt throughout the acquired volumes. However, folding of mirror image artifacts in the OCT FOV resulted in RPE segmentation errors. Moreover, as explained in Section 2.7, the limited number of automatically extracted anatomical landmarks limited the mosaicking accuracy. While the inclusion of manually-extracted landmarks improved the final registration results, it increased the overall processing time, and was prone to placement errors. The cross-correlation maps demonstrated good registration and mosaicking performance. However, the accuracy of our method may be further improved by the introduction of new landmarks, such as inflection points along the retinal and choroidal vasculature. Additionally, complete automation of the landmark extraction step may minimize landmark placement errors and reduce overall processing time.

5. Conclusion

We demonstrated novel multimodality wide-field imaging, and multi-volumetric registration and mosaicking using SECTR. Future developments in swept-source laser, digitizer, and storage technology may be directly implemented to improve SECTR imaging resolution and speed. To the best of our knowledge, this is the fastest implementation of simultaneous *en face* and cross-sectional multimodality imaging to date, and the technology has broad potential applications in *in vivo* imaging in research, commercial, and clinical settings.

Supplementary Material

Refer to Web version on PubMed Central for supplementary material.

Acknowledgments

We thank Castor Optics for providing a prototype 1060 nm double-clad fiber coupler. The work described in this manuscript was performed in part at Cleveland Clinic.

Funding: This research was supported by US National Institutes of Health grant R01-EY023039 and Ohio Department of Development TECH-13-059. The content is solely the responsibility of the authors and does not necessarily represent the official views of the National Institutes of Health.

References

1. Huang D, Swanson EA, Lin CP, Schuman JS, Stinson WG, Chang W, Hee MR, Flotte T, Gregory K, Puliafito CA. Science. 1991; 254:1178–1181. [PubMed: 1957169]
2. Leitgeb R, Hitzenberger CK, Fercher AF. Opt Express. 2003; 11:889–894. [PubMed: 19461802]
3. Choma MA, Sarunic MV, Yang C, Izatt JA. Opt Express. 2003; 11:2183–2189. [PubMed: 19466106]
4. Wojtkowski M, Leitgeb R, Kowalczyk A, Bajraszewski T, Fercher AF. J Biomed Opt. 2002; 7:457–463. [PubMed: 12175297]
5. Wojtkowski M, Srinivasan VJ, Ko TH, Fujimoto JG, Kowalczyk A, Duker JS. Opt Express. 2004; 12:2404–2422. [PubMed: 19475077]
6. Klein T, Wieser W, Reznicek L, Neubauer A, Kampik A, Huber R. Biomed Opt Express. 2013; 4:1890–1908. [PubMed: 24156052]
7. Carrasco-Zevallos OM, Keller B, Viehland C, Shen L, Waterman G, Todorich B, Shieh C, Hahn P, Farsiu S, Kuo AN, Toth CA, Izatt JA. Sci Rep. 2016; 6:31689. [PubMed: 27538478]
8. Kang JU, Huang Y, Zhang K, Ibrahim Z, Cha J, Lee WPA, Brandacher G, Gehlbach PL. J Biomed Opt. 2012; 17:0814031–0814036.
9. Wieser W, Draxinger W, Klein T, Karpf S, Pfeiffer T, Huber R. Biomed Opt Express. 2014; 5:2963–2977. [PubMed: 25401010]
10. Choi SH, Kim WH, Lee YJ, Lee H, Lee WJ, Yang JD, Shim JW, Kim JW. J Opt Soc Korea. 2011; 15:61–67.
11. Veilleux I, Spencer JA, Biss DP, Cote D, Lin CP. IEEE J Sel Top Quantum Electron. 2008; 14:10–18.
12. Rajadhyaksha M, Anderson RR, Webb RH. Appl Opt. 1999; 38:2105–2115. [PubMed: 18319771]
13. Iftimia N, Ferguson RD, Mujat M, Patel AH, Zhang EZ, Fox W, Rajadhyaksha M. Biomed Opt Express. 2013; 4:680–695. [PubMed: 23667785]
14. Izatt JA, Swanson EA, Fujimoto JG, Hee MR, Owen GM. Opt Lett. 1994; 19:590–592. [PubMed: 19844382]
15. Handbook of Biological Confocal Microscopy. James Pawley; Springer: n.d
16. Terhorst D, Maltusch A, Stockfleth E, Lange-Asschenfeldt S, Sterry W, Ulrich M, Lange-Asschenfeldt B. Wound Repair Regen. 2011; 19:671–679. [PubMed: 22092837]
17. Guitera P, Pellacani G, Longo C, Seidenari S, Avramidis M, Menzies SW. J Invest Dermatol. 2009; 129:131–138. [PubMed: 18633444]
18. Flores ES, Cordova M, Kose K, Phillips W, Rossi A, Nehal K, Rajadhyaksha M. J Biomed Opt. 2015; 20:61103. [PubMed: 25706821]
19. Scarff CE. Australas J Dermatol. 2009; 50:152–152.
20. Ntziachristos V. Nat Methods. 2010; 7:603–614. [PubMed: 20676081]
21. Hughes, RC., Alessi-Fox, C. Reflectance Confocal Microscopy. A.N.C. MD, C.M. gro MD, and rtin C.M.J. MD, Melanocytic Prolif. , editor. John Wiley & Sons, Inc.; 2014. p. 474-487.
22. Rajadhyaksha M, Grossman M, Esterowitz D, Webb RH, Anderson RR. J Invest Dermatol. 1995; 104:946–952. [PubMed: 7769264]
23. Klein T, Wieser W, Eigenwillig CM, Biedermann BR, Huber R. Opt Express. 2011; 19:3044–3062. [PubMed: 21369128]

24. Camino A, Zhang M, Dongye C, Pechauer AD, Hwang TS, Bailey ST, Lujan B, Wilson DJ, Huang D, Jia Y. Quant Imaging Med Surg. 2016; 6:391–401. [PubMed: 27709075]
25. Kraus MF, Potsaid B, Mayer MA, Bock R, Baumann B, Liu JJ, Hornegger J, Fujimoto JG. Biomed Opt Express. 2012; 3:1182–1199. [PubMed: 22741067]
26. Zang P, Liu G, Zhang M, Dongye C, Wang J, Pechauer AD, Hwang TS, Wilson DJ, Huang D, Li D, Jia Y. Biomed Opt Express. 2016; 7:2823–2836. [PubMed: 27446709]
27. Lezama J, Mukherjee D, McNabb RP, Sapiro G, Kuo AN, Farsiu S. Biomed Opt Express. 2016; 7:4827–4846. [PubMed: 28018709]
28. Chen Y, Hong YJ, Makita S, Yasuno Y. Biomed Opt Express. 2017; 8:1783–1802. [PubMed: 28663866]
29. LaRocca F, Nankivil D, Farsiu S, Izatt JA. Biomed Opt Express. 2013; 4:2307–2321. [PubMed: 24298396]
30. Choi S, Kim P, Boutilier R, Kim MY, Lee YJ, Lee H. Opt Express. 2013; 21:23611–23618. [PubMed: 24104273]
31. Tanaami T, Otsuki S, Tomosada N, Kosugi Y, Shimizu M, Ishida H. Appl Opt. 2002; 41:4704–4708. [PubMed: 12153106]
32. Wang E, Babbey CM, Dunn KW. J Microsc. 2005; 218:148–159. [PubMed: 15857376]
33. Boudoux C, Yun S, Oh W, White W, Iftimia N, Shishkov M, Bouma B, Tearney G. Opt Express. 2005; 13:8214–8221. [PubMed: 19498851]
34. Schlachter SC, Kang D, Gora MJ, Vacas-Jacques P, Wu T, Carruth RW, Wilsterman EJ, Bouma BE, Woods K, Tearney GJ. Biomed Opt Express. 2013; 4:1636–1645. [PubMed: 24049684]
35. Tearney GJ, Webb RH, Bouma BE. Opt Lett. 1998; 23:1152–1154. [PubMed: 18087457]
36. Tao YK, Farsiu S, Izatt JA. Biomed Opt Express. 2010; 1:431–440. [PubMed: 21258478]
37. Malone JD, El-Haddad MT, Bozic I, Tye LA, Majeau L, Godbout N, Rollins AM, Boudoux C, Joos KM, Patel SN, Tao YK. Biomed Opt Express. 2017; 8:193–206. [PubMed: 28101411]
38. Glazowski C, Rajadhyaksha M. J Biomed Opt. 2012; 17:0850011–0850015.
39. Montigny ED, Madore WJ, Ouellette O, Bernard G, Leduc M, Strupler M, Boudoux C, Godbout N. Opt Express. 2015; 23:9040–9051. [PubMed: 25968739]
40. Wilson T 1, Carlini AR. Opt Lett. 1987; 12:227–229. [PubMed: 19738847]
41. Ryu SY, Choi HY, Na J, Choi ES, Lee BH. Opt Lett. 2008; 33:2347–2349. [PubMed: 18923618]
42. Liang S, Saidi A, Jing J, Liu G, Li J, Zhang J, Sun C, Narula J, Chen Z. J Biomed Opt. 2012; 17:0705011–0705013.
43. Olsovsky C, Hinsdale T, Cuenca R, Cheng YSL, Wright JM, Rees TD, Jo JA, Maitland KC. J Biomed Opt. 2017; 22:056008–056008.
44. Lemire-Renaud S, Strupler M, Benboujja F, Godbout N, Boudoux C. Biomed Opt Express. 2011; 2:2961–2972. [PubMed: 22076259]
45. Vašiček A. JOSA. 1947; 37:623–634.
46. Lane PM. Appl Opt. 2009; 48:5802–5810. [PubMed: 19844318]
47. Martinez-Conde S, Macknik SL, Troncoso XG, Hubel DH. Trends Neurosci. 2009; 32:463–475. [PubMed: 19716186]
48. Dhalla AH, Shia K, Izatt JA. Biomed Opt Express. 2012; 3:3054–3066. [PubMed: 23243559]
49. Pomerantzeff O, Pankratov M, Wang GJ, Dufault P. Am J Optom Physiol Opt. 1984; 61:166–176. [PubMed: 6720862]
50. Wang Z, Lee HC, Ahsen OO, Lee B, Choi W, Potsaid B, Liu J, Jayaraman V, Cable A, Kraus MF, Liang K, Hornegger J, Fujimoto JG. Biomed Opt Express. 2014; 5:2931–2949. [PubMed: 25401008]
51. Choi W, Potsaid B, Jayaraman V, Baumann B, Grulkowski I, Liu JJ, Lu CD, Cable AE, Huang D, Duker JS, Fujimoto JG. Opt Lett. 2013; 38:338–340. [PubMed: 23381430]
52. Poddar R, Raju P, Cortés DE, Werner JS, Mannis MJ, Zawadzki RJ. J Biomed Opt. 2013; 18:86002. [PubMed: 23912759]

53. Arganda-Carreras, I., Sorzano, COS., Marabini, R., Carazo, JM., Ortiz-de-Solorzano, C., Kybic, J. Comput Vis Approaches Med Image Anal. Springer; Berlin, Heidelberg: 2006. Consistent and Elastic Registration of Histological Sections Using Vector-Spline Regularization; p. 85-95.

54. ANSI Z136.1 - Safe Use of Lasers - LIA. https://www.lia.org/publications/ansi/Z136-1

55. Fechtig DJ, Grajciar B, Schmoll T, Blatter C, Werkmeister RM, Drexler W, Leitgeb RA. Biomed Opt Express. 2015; 6:716. [PubMed: 25798298]

56. Goldberg BD, Vakoc BJ, Oh WY, Suter MJ, Waxman S, Freilich MI, Bouma BE, Tearney GJ. Opt Express. 2009; 17:16957–16968. [PubMed: 19770914]

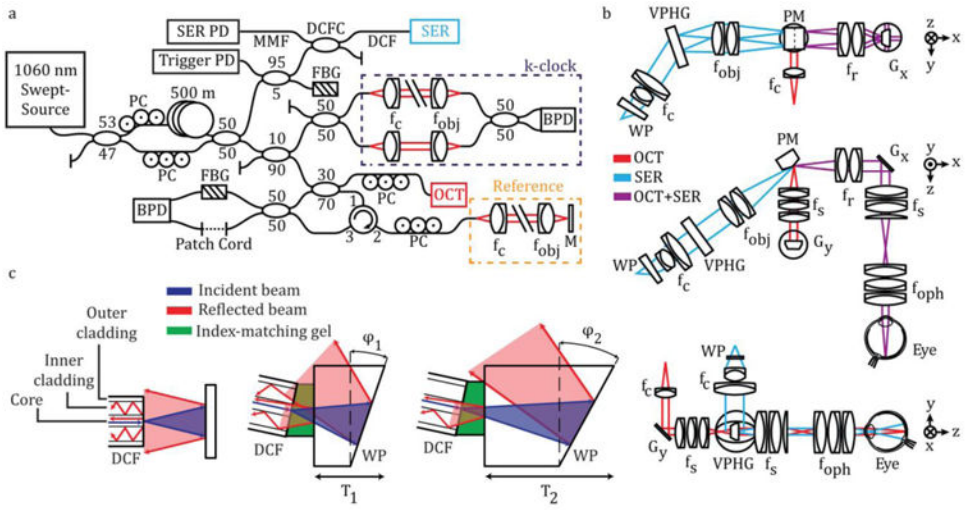

Figure 1.

SECTR system schematic. (a) A 1060 nm swept-laser source was optically buffered and split between OCT and SER arms. One output of the buffering stage was split for OCT and k-clock, and the path was subsequently split between a reflective reference and sample arms. The second output of the buffering stage coupled SER illumination to a DCF coupler for single-mode illumination and multimode detection through the core and inner-cladding of the DCF, respectively. FBGs in the SER and OCT arms were used to generate a wavelength-specific trigger and remove phase-noise from laser sweep jitter, respectively. (b) Orthogonal cross-sections showing SECTR beam paths and imaging optics (OCT, red; SER, blue; shared OCT+SER, purple). OCT and SER paths were combined by a prism mirror and shared a galvanometer scanner (G_x: OCT fast-axis and SER scan axis). (c) Schematics showing back-coupling of end-face reflections in a DCF from the fiber-air interface and a downstream air-glass interface (left). Both reflections were reduced by coupling the DCF to a wedge-prism (WP) with thickness, T_1, and wedge angle, φ_1, (middle) and were minimized for T_2 and φ_2 (right). BPD, balanced photodiode; f, collimating, objective, ophthalmic, relay, and scan lenses; $G_{x,\,y}$, galvanometer scanners; M, mirror; MMF, multimode fiber; PC, polarization controller; PD, photodiode; PM, prism mirror; VPHG, grating.

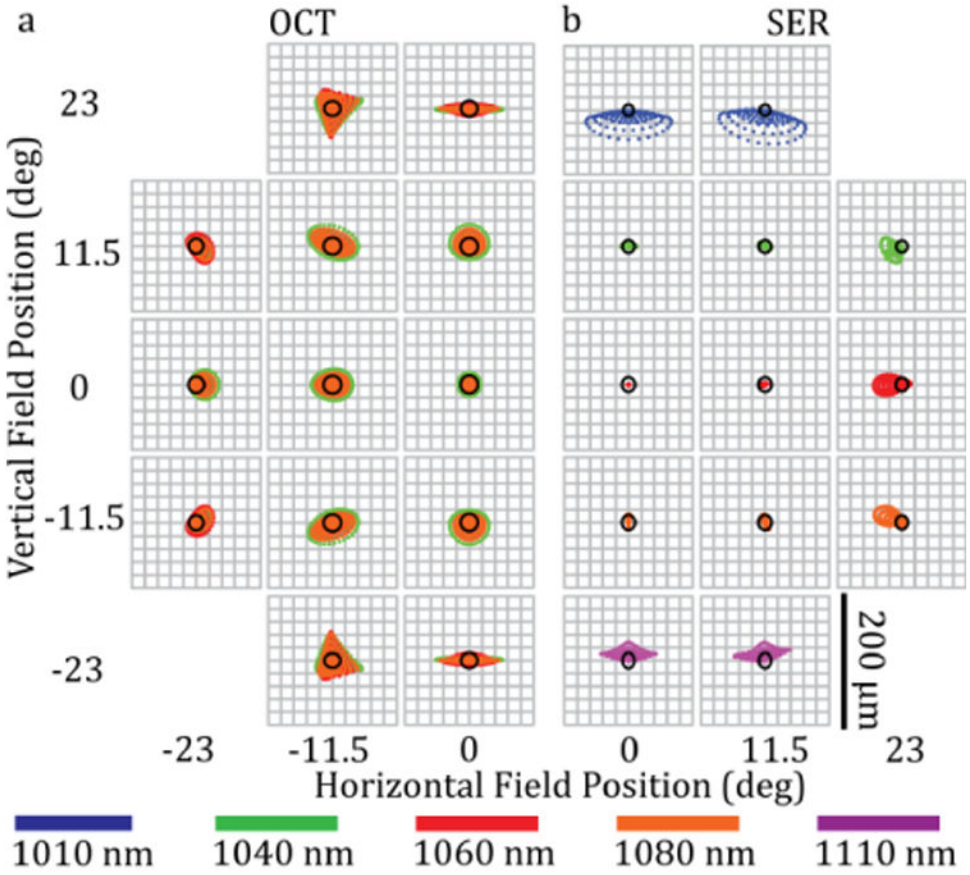

Figure 2.

SECTR ZEMAX spot diagram. Spot matrix for (a) OCT and (b) SER showing the full circular FOV simulated at the retina. The FOV was symmetric and only half-fields are shown for each modality. (a) OCT spots were diffraction-limited on-axis, whereas (b) SER spots were diffraction- and near diffraction-limited within the central 23° of the field. The Airy radius was 13 and 10.5 μm for OCT and SER, respectively.

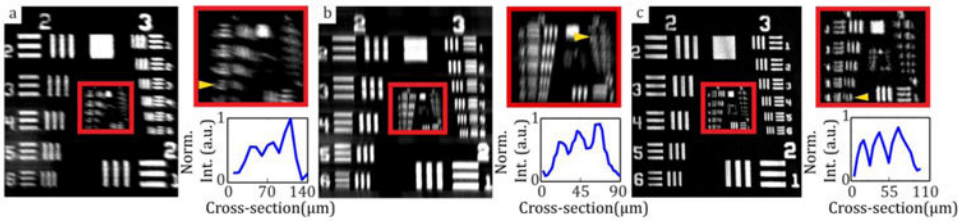

Figure 3.

SECTR lateral resolution characterization. (a) *En face* OCT volume projection and magnified region showing contrast cross-section (inset) of group 4, element 6 (arrow, 35 μm). (b), (c) Two SER images were acquired at offset image planes to compensate for slight astigmatism at the focus. SER images and contrast cross-sections with the (b) spectrally-encoded and (c) scanned dimensions in focus showing group 4, element 5 (arrow, 39 μm) and group 5, element 2 (arrow, 28 μm), respectively. Anisotropic SER lateral resolution is a result of dominant chromatic aberration.

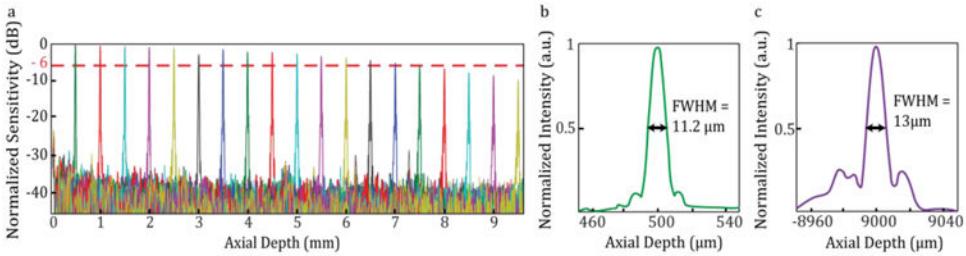

Figure 4.

OCT fall-off plot showing SNR and axial point spread function measurements. (a) A -6 dB fall-off depth of 7.5 mm and full imaging range of 9.56 mm were measured when imaging with a 1.2 GHz k-clock. (b) The FWHM of the axial PSF in air was between 11-13 μm across the full imaging range.

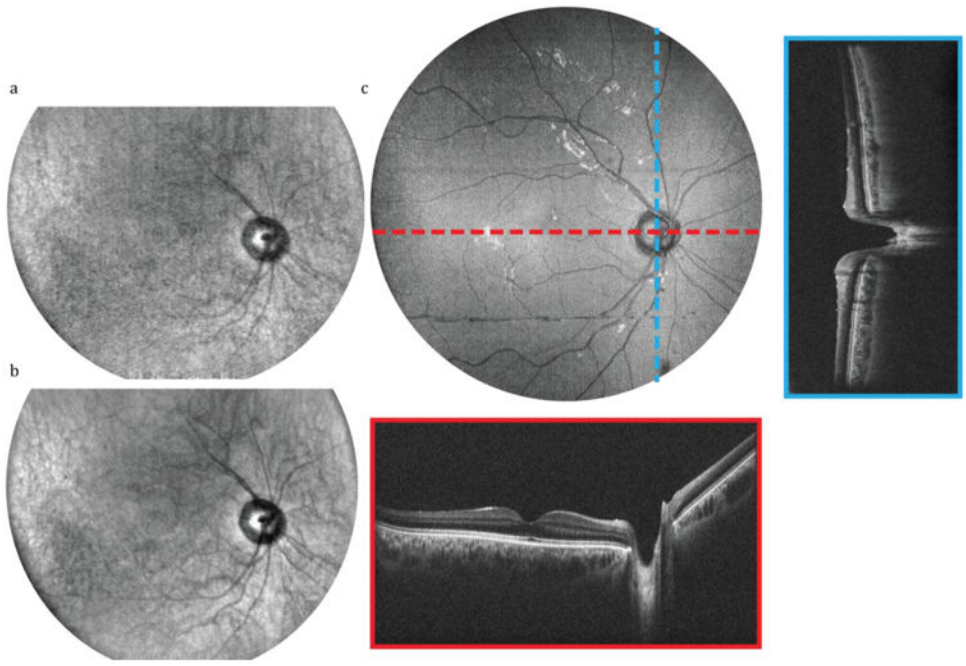

Figure 5.

In vivo SECTR imaging of the posterior retina with >45° (15 mm) FOV in a healthy volunteer (Visualization 1). (a) Raw and (b) 5-frame average of 2560 × 2000 pix. (spectral × lateral) SER images acquired at 200 fps. (c) *En face* OCT volume projection with representative 5-frame averaged fast- and slow-axis cross-sections (red and blue, respectively). OCT volume was sampled with 2560 × 2000 × 1400 pix. (spectral × lateral × lateral) in 7 s.

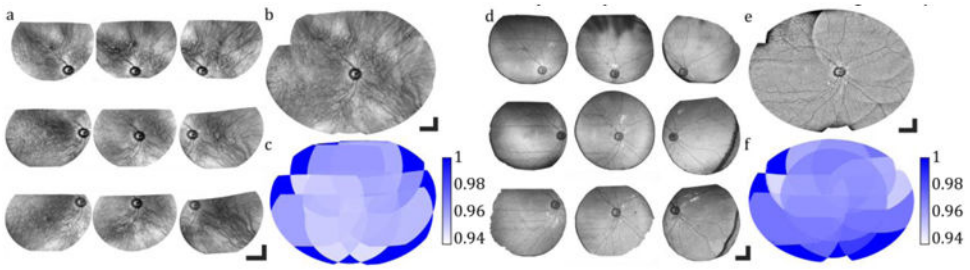

Figure 6.

SECTR multi-volumetric mosaicking. (a)SER and (d) OCT sub-fields after multi-volumetric and non-rigid transformation (b) SER and (e) OCT wide-field multi-volumetric mosaics. (c), (f) Validation map representing cross-correlation coefficients after mosaicking. Scale bars: 10°.

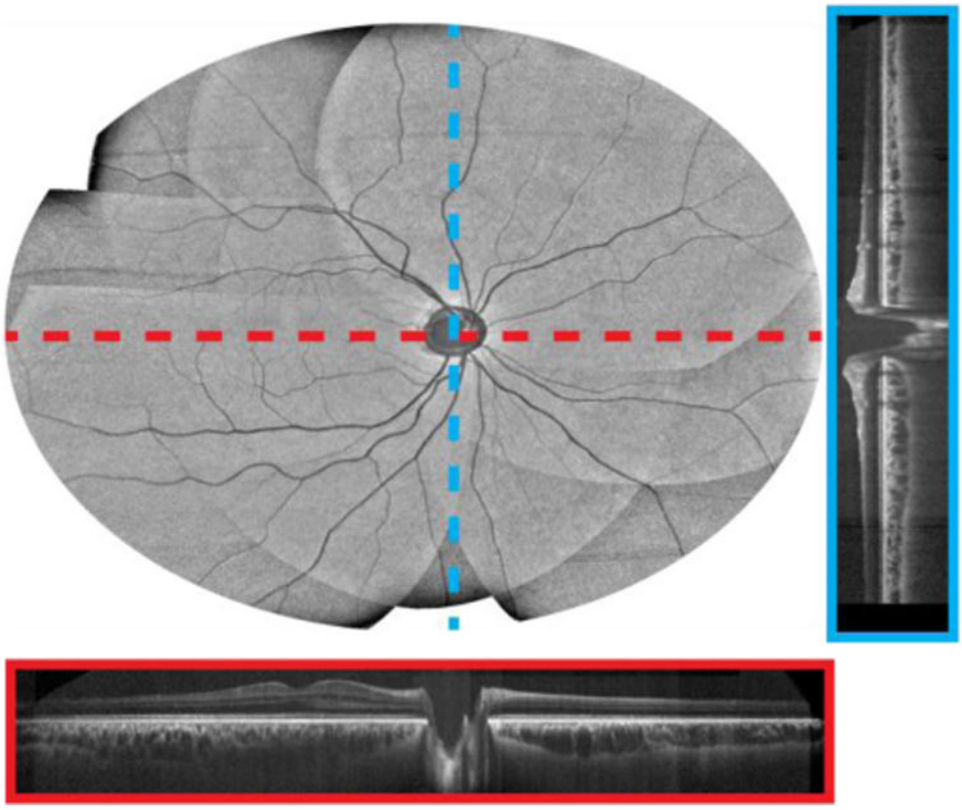

Figure 7.

Multi-volumetric mosaic of the posterior retina with a 90° FOV. *En face* OCT volume with representative fast- and slow-axis cross-sections (red and blue, respectively) after flattening, registration, and mosaicking.

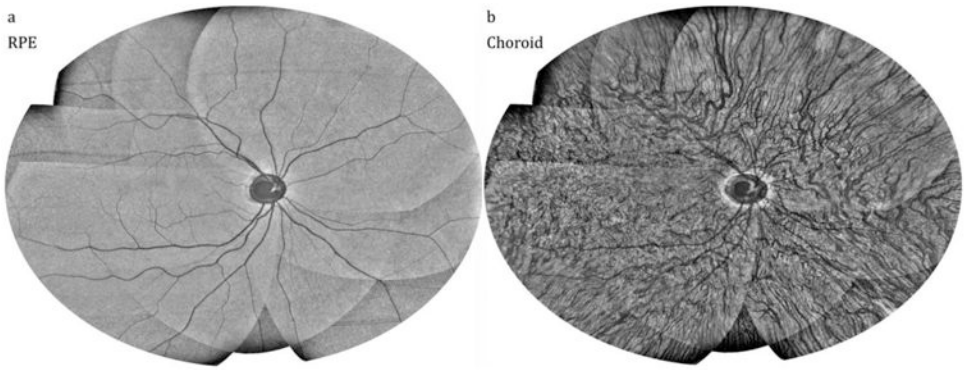

Figure 8.

En face multi-volumetric OCT mosaics at different retinal layers. (a) 20-frame average in depth around the RPE and (b) 25-frame average in depth in the choroid.